ELSEVIER

Morphological interpretation of *n*-hexane diffusion in polyethylene ☆

A. Mattozzi, B. Neway, M.S. Hedenqvist, U.W. Gedde*

Fibre and Polymer Technology, Royal Institute of Technology, SE-100 44 Stockholm, Sweden

Abstract

The diffusion of small-molecule penetrants in polyethylene is retarded by the detour caused by the crystals and by the segmental constraints imposed by the crystals on the penetrable phase. The earlier reported *n*-hexane diffusivity data for a series of homogeneous poly(ethylene-*co*-octene)s showed unexpectedly that the detour was greatest in the low crystallinity polymers. The crystal width-to-thickness ratio and the crystallinity were assessed by electron microscopy and differential scanning calorimetry and used in the Fricke model. The calculations showed that the geometrical impedance factor followed the same trend with increasing crystallinity as the data obtained from *n*-hexane desorption. The high geometrical impedance factor shown by the low crystallinity samples was due to the presence of crystals with an unusually high crystal width-to-thickness ratio. A unified relationship, including data for both linear and branched polyethylene was found between the fractional free volume and the phase composition of the penetrable phase including the liquid-like, interfacial liquid and the interfacial crystal core.
© 2004 Elsevier Ltd. All rights reserved.

1. Introduction

The penetration of small-molecule penetrants is restricted to the non-crystalline fraction in semicrystalline polymers. The crystal phase of linear polyethylene is densely packed and only the smallest penetrant molecules such as helium can penetrate the crystals [1]. The trajectories of the penetrant molecules are extended by the crystallites with respect to those in the fully amorphous analogue for a given displacement. This extension of the diffusive path has been described by the geometrical impedance factor (τ):

$$\tau = \frac{D_a}{D\beta} \tag{1}$$

where D_a is the penetrant diffusivity in the fully amorphous analogue, D is the diffusivity in the semicrystalline polymer and β is a factor taking into account the segmental

constraints imposed by the crystal on the penetrable fraction of the polymer. Essentially all the amorphous chain segments have one or both ends anchored in the crystals. The segmental mobility is thereby lowered with respect to the fully amorphous analogue. Proof of the deviation from the liquid-like behaviour of the rubbery amorphous component of polyethylene has been found by proton NMR [2] and Raman spectroscopy [3]. The two effects of the crystals on the diffusivity—the extended diffusive path and the constraint of the amorphous chains—are conveniently separated by the free volume theory of Cohen and Turnbull [4,5] and Fujita [6]:

$$D_T = A \times \exp(-B_d/f_2)$$
$$\times \exp((B_d \nu_1^a (f_1 - f_2))/(f_2(f_2 + \nu_1^a (f_1 - f_2)))) \tag{2}$$

where D_T is the penetrant thermodynamic diffusivity, A is a factor that is inversely proportional to τ, B_d is a constant that depends only on the size and shape of the penetrant molecule [7], ν_1^a is the volume fraction of penetrant in the penetrable phase, f_1 is the fractional free volume of the penetrant and f_2 is the fractional free volume of the penetrable fraction of the polymer. The product of the first

two factors in Eq. (2) constitutes the zero-concentration diffusivity. The third factor describes the increase in the diffusivity with increasing penetrant concentration. It should be pointed out that Eq. (2) is applicable only to systems with a constant volume of mixing (ΔV), i.e. $\Delta V = V_{mix} = (V_p + V_{pen}) = 0$; where V_{mix} is the volume of the mixed system, V_p is the volume of the polymer and V_{pen} is the volume of the penetrant.

Numerically, Eq. (2) describes the desorption of n-hexane in polyethylene extremely well [7–12]. Neway et al. [9] showed that Eq. (2) gives physically feasible results only for the free volume scale according to Doolittle [13], Williams et al. [14] and Cohen and Turnbull [4], i.e. a scale with a fractional free volume at the glass transition temperature of ~ 0.02–0.03. The fractional free volume (f_1) used for n-hexane was, according to Fleischer [12], $f_1 = 0.168$, which yields fractional free volumes for amorphous polyethylene consistent with a fractional free volume of 0.025 at the glass transition temperature.

This paper is a follow-up of previous papers [9,15], which presented data for the fractional free volume of the penetrable component (f_2) and the geometrical impedance factor (τ) of linear polyethylene and homogeneous poly-(ethylene-*co*-octene)s based on n-hexane desorption data using Eq. (2) to describe the concentration-dependent diffusivity. Fig. 1 shows the dependence of the geometrical factor A (inversely proportional to τ) on the degree of crystallinity for the homogeneous poly(ethylene-*co*-octene)s. The unexpected trend in the A data, i.e. that the geometrical impedance factor increases with decreasing crystallinity, is the main theme of this paper and it is given a morphological explanation based on the results obtained by differential scanning calorimetry and transmission electron microscopy. It is shown that the crystal width-to-thickness ratio is the main factor; the crystals in the samples with low crystallinity showing a very high crystal width-to-thickness ratio.
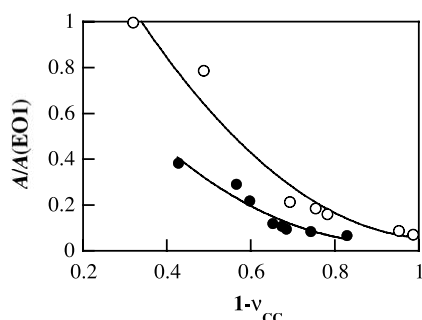
The paper also considers the free volume effect of the crystallinity and degree of branching. Fig. 2 presents a summary of the effect of the degree of crystallinity on f_2. The poly(ethylene-*co*-octene)s show a pronounced increase in f_2 with decreasing crystallinity whereas linear poly-ethylene exhibits only a small change in f_2 with changing crystallinity (Fig. 2). Linear and branched polyethylenes with a 40% crystallinity show different f_2 values: 0.042 (linear polyethylene) and 0.052 (poly(ethylene-*co*-octene)s). The f_2 data for the two groups of polymers converge at a high degree of crystallinity. This interesting difference in behaviour between linear and branched polyethylene is also discussed in this paper.

2. Experimental

2.1. Materials

The homogeneous poly(ethylene-*co*-octene)s, denoted EOX$_{hex}$ where X_{hex} is the percentage molar fraction of hexyl branches in the polymer, were synthesized using a boron-activated metallocene catalyst in a continuously stirred tank reactor. The molar mass distribution characteristics of the polymers (with one exception) were according to size exclusion chromatography: $\bar{M}_w = 80,000 \pm 10,000$ g mol^{-1} and $\bar{M}_w/\bar{M}_n = 2.1 - 2.5$. For EO2.3, the following molar mass data were obtained: $\bar{M}_w = 54,000$ g mol^{-1} and $\bar{M}_w/\bar{M}_n = 1.9$. The polymers were compression moulded to discs, 30 mm in diameter and 1 mm thick, in a Schwabentan Polystat 400s compression moulding machine at 433 K under a pressure of 10 MPa for 5 min followed by cooling at 0.2 K min^{-1} to 298 K while the pressure was maintained.
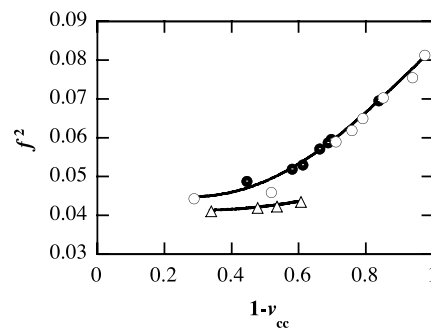

Fig. 1. Geometrical factor A normalized with respect to the value for the sample with the highest degree of crystallinity as a function of volume fraction of non-crystalline phase (v_{cc} is the volume fraction of crystal core component) for homogeneous poly(ethylene-*co*-octene) (○) and hetero-geneous poly(ethylene-*co*-octene) (●). The method used to obtain A assumed that the interfacial crystal core, the interfacial liquid-like and the liquid-like components were penetrable. The continuous lines are third degree polynomial fits to the experimental data. From Neway et al. [15] with permission from Elsevier.

Fig. 2. Fractional free volume of the penetrable polymer fraction (f_2) as a function of volume fraction of non-crystalline phase (v_{cc} is the volume fraction of crystal core component) for linear polyethylene (△), homogeneous poly(ethylene-*co*-octene)s (○) and heterogeneous poly-(ethylene-*co*-octene)s (●). The method used to obtain f_2 assumed that the interfacial crystal core, the interfacial liquid-like and the liquid-like components were penetrable. The continuous lines are polynomial fits (linear polyethylenes-second degree; poly(ethylene-*co*-octene)s-forth degree) to the experimental data. Drawn after data from Neway et al. [9, 10,15].

The compression moulding was the same as that used in a previous study on the same polymers [15].

2.2. Methods

All the characterizations described in this section were made on samples given a thermal treatment according to Section 2.1. Melting traces were recorded at a heating rate of 10 K min^{-1} on 5 ± 1 mg samples in a Mettler-Toledo DSC 820 with nitrogen as purge gas. Three samples for each material were tested. The mass crystallinity (w_c) was obtained from data for the heat of fusion (Δh_f) using the total enthalpy method [16]:

$$w_c = \frac{\Delta h_f}{\Delta h_f^0 - \int_{T_1}^{T_m^0} (c_{p,a} - c_{p,c})dT} \quad (3)$$

where T_1 is an arbitrary temperature below the melting range, $c_{p,a}$ and $c_{p,c}$ are, respectively, the specific heats of the amorphous and the crystalline phases, and $\Delta h_f^0 = 293$ kJ kg^{-1} is the heat of fusion for 100% crystalline polyethylene at the equilibrium melting point (($T_m^0 = 418.7$ K) [17]). Data for $c_{p,a}$ and $c_{p,c}$ from Wunderlich and Baur [18] have been used. Crystal thickness data were obtained for the different polymers from the melting peak temperatures using the Thomson–Gibbs equation [19].

The average spherulite radius ($\langle r_s \rangle$) was assessed by small-angle light scattering on 50 μm thick microtomed sections of the materials and was calculated according to Pakula et al. [20]:

$$\langle r_s \rangle = \frac{4.09\lambda}{4\pi n \sin\left(\frac{\theta_{max}}{2}\right)} \quad (4)$$

where θ_{max} is the scattering angle corresponding to the maximum in scattered intensity, $\lambda = 617.6$ nm is the wavelength of the light (Marwell M1805-P, 5 mW He-Ne-laser) and $n = 1.5$ is the average refractive index of the polymer. The scattering angle at the scattered intensity maximum (θ_{max}) was obtained by visual examination of the scattering pattern recorded on a photographic film. The superstructure of the samples was determined by polarized microscopy on 50 μm thick microtomed sections of the material in a Leitz Ortholux II POL-BK optical microscope.

The lamellar structure was studied in a Tecnai 10 100 kV transmission electron microscope on etched samples. The permanganic etching was carried out using the etchant recipes developed by Shahin et al. [21]: samples were etched at room temperature for either 5 or 20 h in two different reagents: (i) 1 g/l potassium permanganate in a mixture of 2 parts by volume of concentrated sulphuric acid and 1 part by volume of orthophosphoric acid (99%); (ii) 1 g/l potassium permanganate in a mixture of 10 parts by volume of concentrated sulphuric acid, 4 parts by volume of orthophosphoric acid (99%) and 1 part by volume of water.

The samples were subsequently washed, replicated in two stages using cellulose acetate for the first impression, shadowed with Au/Pd in a vacuum evaporator, coated with carbon, transferred to a copper grid and examined in the transmission electron microscope. The nitric acid digestion was performed on 5 mg samples at 333 K in fuming nitric acid for 9 days, washed and ultra-sonicated for 10 min in 5 ml of distilled water. A drop of the suspension of crystals in distilled water was collected with a pipette and laid on a carbon-Formvar coated grid; after the water had evaporated, the grids were shadowed with Au/Pd in a vacuum evaporator and examined in the transmission electron microscope.

3. Results and discussion

3.1. Morphology and geometrical impedance factor

Table 1 presents the crystallinities obtained by differential scanning calorimetry and those assessed with Raman spectroscopy and density measurements; the latter two have been reported earlier [15]. Raman spectroscopy provided information about the fractions of crystal-core (CC), interfacial crystal-core (ICC), interfacial liquid-like (IL), and liquid-like (L) components according to Mutter et al. [3]. The crystallinities obtained by calorimetric measurements were in agreement with the crystallinities based on density data. As shown elsewhere [8], the crystallinities based on calorimetric measurements were between the mass fractions of crystal core and the sum of the crystal core and interfacial crystal core components obtained by Raman spectroscopy. The crystallinity of sample EO2.3 was much higher than that of EO2.4 although the comonomer content differed by only 0.1%. It is possible that the low molar mass of EO2.3 is responsible for its relatively high crystallinity.

Polarized microscopy provided information about the supermolecular structure. The samples with a low degree of branching ($\leq 2.4\%$) showed a spherulitic superstructure. Samples EO3.6 and EO4.3 showed a random lamellar structure. These findings were substantiated by the data obtained by small-angle light scattering: the samples with a lower degree of branching ($\leq 2.4\%$) showed clover-leaf patterns typical of spherulites, whereas the samples with a higher degree of chain branching showed azimuthal-angle-independent scattering, indicative of a random lamellar structure. Sample EO2.3 showed distinctly larger spherulites than the other samples, also in this case due to its low molar mass. The spherulite radius data obtained by small-angle light scattering are presented in Table 2.

The Thomson–Gibbs equation [19] was used to convert the peak melting temperature (T_m) to crystal thickness (L_c):

$$T_m = T_m^0(p) \times \left[1 - \frac{2\sigma(p)}{\Delta h_f^0 \rho_c L_c}\right] \quad (5)$$

Table 1
Crystallinity and phase composition according to Raman spectroscopy

Sample	w_c[a]	w_c[b]	w_{CC}[c]	w_{ICC}[c]	w_{IL}[c]	w_L[c]
EO0.4	0.78	0.72	0.72	0.071	0.052	0.162
EO0.8	0.56	0.57	0.55	0.099	0.092	0.257
EO1.9	0.43	0.41	0.34	0.135	0.111	0.414
EO2.3	0.38	0.38	0.27	0.143	0.130	0.453
EO2.4	0.36	0.35	0.24	0.150	0.113	0.493
EO3.6	0.20	0.22	0.06	0.136	0.136	0.672
EO4.3	0.14	0.17	0.02	0.149	0.128	0.705

[a] Calculated from data obtained by differential scanning calorimetry according to Eq. (3).
[b] By density measurements weighing the samples in air and ethanol and applying the Archimedes principle. Data from Neway et al. [15].
[c] By Raman spectroscopy. Data from Neway et al. [15].

where $T_m^0(p)$ is the equilibrium melting point for the copolymer with p molar fraction of crystallizable units, $\sigma(p)$ is the specific free energy of the fold surface for the copolymer with p molar fraction of crystallizable units—for linear polyethylene it is equal to 93 mJ m^{-2} [22]—and ρ_c is the crystal phase density, which for linear polyethylene at 295 K is equal to 996 kg m^{-3} [23]. Defoor et al. [24] reported a moderate increase in the unit cell volume for fractions of poly(ethylene-co-octene)s with increasing degree of chain branching: 93.5 Å^3 (linear polyethylene) to 96.2 Å^3 for a copolymer with 2.8% hexyl branches. These samples crystallized during a 5 K min^{-1} cooling from the melt. Thus, the crystal density showed a variation between 967 and 996 kg m^{-3}. The use of a universal value, $\rho_c = 996$ kg m^{-3}, in the calculation of crystal thickness according to Eq. (5) gives thus a maximum error of 3%.

The equilibrium melting points of the copolymers were calculated according to [25]:

$$T_m^0(p) = \frac{1}{\left(\dfrac{1}{T_m^0(p=1)} - \dfrac{R}{\Delta H_{f,r}^0} \times \ln p\right)} \quad (6)$$

where $\Delta H_{f,r}^0$ is the heat of fusion per mole of crystallizable repeating unit, which for polyethylene is equal to 4.1 kJ

(mole CH$_2$ units)$^{-1}$ [17]. Eq. (6) assumes that the branches are excluded from the crystals. Hay and Zhou [26] found that a small fraction ($\sim$10%) of hexyl branches are included in the crystals. However, they stated that the results were only relevant for quenched crystallization and that crystallization during slower cooling most likely would lead to a lower degree of incorporation of the hexyl branches in the crystals. Similar results were obtained by Hosoda et al. [27]. They reported for quenched samples that the concentration of hexyl-branches in the crystal phase was only 6% of the total branch content. Mathur and Mattice [28] presented data that suggest that hexyl branches are excluded from the crystals. Li and Akpulo [29] reported results on isothermally crystallized butyl-branched polyethylene consistent with the branch-rejection model (Eq. (6)). The incorporation of hexyl-branches in the crystalline component in our samples should be very low in view of the low cooling rate (0.2 K min^{-1}) used during crystallization. The prerequisite for Eq. (6) is thus fulfilled. Data for the calculated equilibrium melting points of the different samples are presented in Table 2.

The specific free energy of the fold surface is another concern. Li and Akpulo [29] obtained in a study of isothermally crystallized poly(ethylene-co-1-hexene) with 6.4 mol% 1-hexene using differential scanning calorimetry

Table 2
Melting points and morphological characteristics of samples

Sample	T_m (K)[a]	$T_m^0(p)$ (K)[b]	$\langle r_s \rangle$ (μm)[c]	L_c (nm)[d]	W (nm)[e]
EO0.4	408.1	417.3	5.4	28.6	609
EO0.8	396.0	415.9	6.1	13.2	516
EO1.9	376.7	412.0	7.0	7.4	325
EO2.3	372.8	410.6	18.2	6.9	568
EO2.4	367.5	410.2	7.3	6.1	513
EO3.6	317; 336[f]	406.1	–[g]	2.9; 3.7 [h]	732
EO4.3	317; 337[f]	403.7	–[g]	3.0; 3.9 [h]	1353

[a] Melting peak temperature obtained by differential scanning calorimetry; average value based on three measurements.
[b] Equilibrium melting temperature calculated according to Eq. (6).
[c] Calculated from data obtained by small-angle light scattering according to Eq. (4).
[d] Calculated from melting peak temperature data according to Eq. (5). The fold surface energy ($\sigma(p)$) was set to 93 mJ m^{-2}.
[e] By transmission electron microscopy of permanganic etched samples.
[f] Two melting peaks.
[g] No clover-leaf pattern.
[h] Two crystallite populations associated with two melting peaks were present.

and small-angle X-ray scattering a value of 90 mJ m^{-2} for the specific fold surface energy. Darras and Séguéla [30] reported a gradual increase in σ with increasing p for rapidly cooled poly(ethylene-*co*-butene)s from 70 mJ m^{-2} for the copolymer with 1 mol% 1-butene to 110 mJ m^{-2} for the copolymer with 7.6 mol% 1-butene. The increase in fold surface energy was attributed to disordering of the fold surface in the highly branched samples. The fold surfaces in the samples of the present study were given time to mature during the very slow cooling used (0.2 K min^{-1}), which induced the use of a universal value, 93 mJ m^{-2}, for all the copolymers. The trends in the obtained data would not be qualitatively different even in the case of an increasing $\sigma(p)$ with decreasing p in accordance with the data of Darras and Séguéla [30].

The melting curves were unimodal with two exceptions (EO3.6 and EO4.3) and the melting peaks were relatively narrow. The peak temperature is thus a good representation of the crystal population. Melting peak temperatures as averages of three measurements are presented in Table 2. Fig. 3 presents crystal thickness data together with data for the average chain length between adjacent chain branches as a function of the degree of branching. The highly branched systems showed crystal thicknesses only slightly less than the average chain length between adjacent branches, whereas for the sample with the lowest degree of chain branching (EO0.4), $L_c \approx \langle L \rangle /2$. The crystal thickness range included in this study is broad, ranging from ca. 3 to 28.6 nm (Table 2). The polymers with the highest degree of chain branching (EO3.6 and EO4.3) showed bimodal melting suggesting a heterogeneous distribution of branches. The difference in crystal thickness associated with the two melting peaks was, however, small (Table 2). The calculated crystal thickness data presented in Table 2 are in accordance with crystal thickness estimates obtained by small-angle X-ray scattering on similar samples [24,29]. Li and Akpalu [29] reported the following melting points and crystal thicknesses for poly(ethylene-*co*-1-hexene) obtained by small-angle X-ray scattering: 343 K—4.3 nm; 387 K—11±2 nm. These data are consistent with our
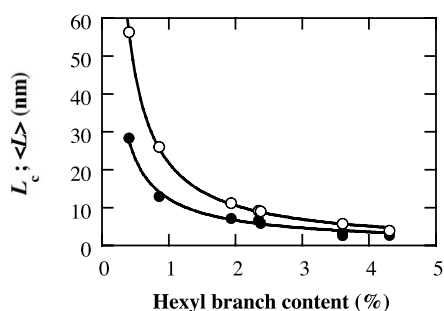
calculated crystal thickness data (Table 2). Defoor et al. [24] reported the following crystal thicknesses obtained by small-angle X-ray scattering of fractions of poly(ethylene-*co*-octene)s crystallized during a 5 K min^{-1}: 0.3% hexyl branches—16.3 nm; 0.6%—13.0 nm; 1.2%—7.0 nm; 2.0%—4.3 nm; 2.8%—2.4 nm. These data are basically consistent with the crystal thickness data reported in Table 2 in view of the difference in cooling rate used during which the different samples crystallized. The crystal thicknesses reported by Defoor et al. [24] are ~60% of the thicknesses reported in Table 2 for samples with corresponding degree of chain branching.

Crystal widths were measured on transmission electron micrographs of replicas of permanganic-etched samples. Crystal width is defined in Fig. 4. Fig. 5 presents a few selected micrographs. The spherulitic morphology in the samples with a low degree of chain branching was also evident in the low magnification electron micrographs (Fig. 5(a)). The samples with low crystallinity showed few but very wide crystal lamellae and no spherulitic order (Fig. 5(b)). These lamellae are almost in the plane of the surface with a vertical **b** axis orientation and a visible {110} tip. Many samples contained S-shaped lamellae (Fig. 5(c)). The particles obtained after nitric acid etching occasionally revealed the true structure of the crystals (Fig. 5(d)). In most cases, however, the particles were only fragments of crystals and they were not useful for the assessment of the crystal width.

In order to obtain a realistic, observer-unbiased value of the crystal width, all the crystal dimensions in every edge-on view were measured and averaged. In this way, the quantity measured is a combination of crystal widths seldom perpendicular to the spherulite growth direction. The relationship between the average size of a lamella in an edge-on view and the true width of the lamella according to Fig. 4 can be calculated considering the shape of the intersection of a plane and a ribbon of width W freely rotating in space. The solution to the
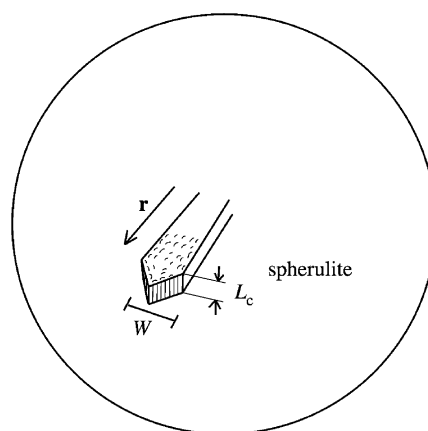

Fig. 3. Crystal thickness (L_c; ○) and average chain length between adjacent chain branches ($\langle L \rangle$; ●) as a function of hexyl branch content given in mol%. The crystal thickness was calculated from Eq. (5) using melting peak temperature data obtained by differential scanning calorimetry. The continuous lines are power law fits to the data.

Fig. 4. Definition of crystal width (W) and crystal thickness (L_c). The spherulite radius is denoted **r**.
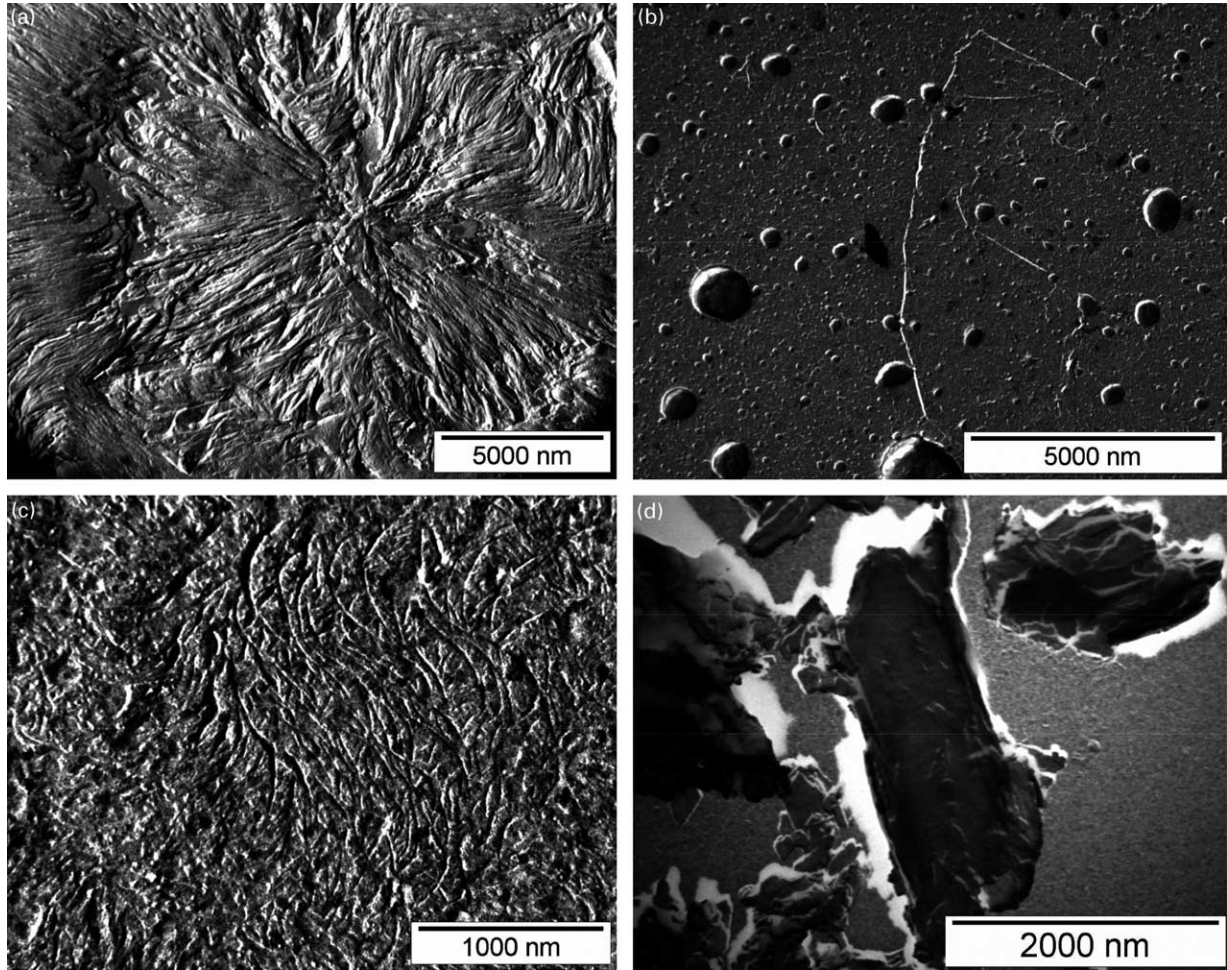
Fig. 5. Transmission electron micrographs of permanganic-etched samples: (a) EO0.4; (b) EO3.6; (c) EO 1.9 and of fragments obtained after nitric acid etching of sample: (d) EO1.9.

problem is the following integral (Appendix A):

$$Q = \frac{4}{\pi^2}$$

$$\times \lim_{t \to 0} \int_{\alpha=t}^{\frac{\pi}{2}} \int_{\beta=0}^{\pi} \cos\left(\text{arctant}\left(\frac{\cos\alpha \sin\beta}{\sin\alpha}\right)\right) d\alpha d\beta$$

$$= 0.74245$$

(7)

The average width data obtained from the micrographs were multiplied by the factor Q to obtain the 'true' average crystal width (Table 2).

The treatment of Michaels and Bixler [31] relating the geometrical impedance factor (τ) to the characteristics of a system of non-penetrable oblate spheroids dispersed in a penetrable continuous matrix, which is based on the theory of Fricke [32] for electric conductivity in a two-component system, was applied to calculate the geometrical impedance factor of the polymers studied:

$$\tau = 1 + \frac{v_c\left[0.384 + \left(0.785 - \frac{L_c}{W}\right)^2\right]}{1.848 - 3\left(0.785 - \frac{L_c}{W}\right)^2}$$

(8)

where v_c is the volume fraction of the crystalline component. A more recent study of Hadgett, Goldbeck-Wood and Windle [33] showed that Monte–Carlo simulation of penetrant diffusion in systems with impenetrable plates gave results in accordance with the Michaels–Bixler version of the Fricke theory. The geometrical impedance factor was calculated using data for the volume crystallinity obtained from mass crystallinity by density measurements (Table 1) and crystal thickness-to-width ratio (L_c/W). The crystallinity based on calorimetric measurements differed on an average only by 0.01 from the density-based crystallinity (Table 1). The difference in the calculated τ values obtained by the two different assessments of crystallinity would be maximum 4% for the sample with the lowest degree of crystallinity. The crystal thickness

average and the whole distribution of crystal widths obtained from the transmission electron micrographs were used in the calculation of L_c/W. From the distribution of the geometrical impedance factor, an average τ value was obtained. For samples showing two separate melting peaks and hence a bimodal distribution of the crystal thickness, the average of the two crystal thicknesses was used. It is important to point out, that, although several hundred lamellae were included in the analysis of each sample, the calculated average in crystal width is associated with considerable uncertainty.

The geometrical impedance factors for the crystalline structures observed are presented in Fig. 6. The highly branched polymers showed very high crystal aspect ratios (W/L_c), and high values of the geometrical impedance factor were thus calculated for these samples. The values of τ obtained by fitting Eq. (2) to the experimental desorption data, earlier reported by Neway et al. [15], showed a trend with respect to crystallinity similar to that shown by the τ data predicted from microscopy data using the Fricke theory. The Fricke theory is thus giving the correct trend in the geometrical impedance factor-crystallinity data (Fig. 6). The calculated τ data were in fair agreement with the data obtained by method II (IL and L are penetrable phases). The discrepancy between the calculated τ values and those obtained by method I (ICC, IL and L are penetrable phases) was significant. However, simple arguments suggest that the analysis based on the Fricke theory has limitations. The crystals are assumed to be oblate spheroids with a certain width and thickness. The real morphology is a highly branched and continuous crystalline structure from the centre to the periphery of each spherulite. The continuity of crystals along the spherulite radius and the difference in the crystal dimensions along the two directions perpendicular to the lamellar normal are aspects not considered in the Fricke theory. A more elaborate model, capable of taking into account both the aforementioned aspects, based on Monte–Carlo simulation of penetrant diffusion through computer-built spherulites, will be reported in a coming paper [34].
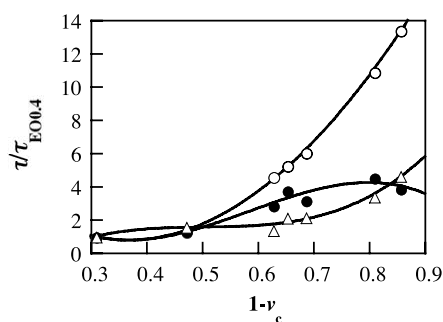

Fig. 6. Geometrical impedance factor normalized with respect to the value for EO0.4 ($\tau/\tau_{EO0.4}$) as a function of volume crystallinity (v_c) obtained from *n*-hexane desorption data (○ Method I; ● Method II) and calculated from Eq. (8) using morphological data (△). The continuous lines are third degree polynomial fits to the data.

Preliminary results suggest that the geometrical impedance factor takes values consistent with the Fricke theory but with an effective crystal aspect ratio considerably greater than that given by W (width according to the **b** view) and L_c.

3.2. Morphology and free volume of penetrable component

This section seeks to provide an explanation of the data presented in Fig. 2. It is possible, by analogy with the mechanical data reported by Boyd [35], that the phase properties of branched polyethylene gradually change with crystallinity. Linear polyethylene shows only a moderate change in f_2 with increasing degree of crystallinity, which is precisely what the relaxation modulus of the amorphous component shows for this material [35].

An alternative approach, not necessarily correct, considers the penetrable phase as a composite consisting of a liquid-like phase resembling the free amorphous phase and an interfacial component with different conformation and reduced fractional free volume. Small-angle X-ray scattering data suggest the existence of a relatively sharp interface between crystal and amorphous phases [36]. This thin layer with a density gradient constitutes only a small fraction of the interfacial component as revealed by NMR [2] and Raman spectroscopy [10]. Hence, most of the interfacial component is composed of material with a liquid-like density but with a restricted mobility and a different chain conformation. According to the composite model, the interfacial component is assumed to trap a given penetrant molecule for a significant fraction of its diffusive time (t_{tr}). The relationship between the fractional free volume of the constrained penetrable polymer in the semicrystalline state (f_2) and t_{tr} is given by (Appendix B):

$$\exp\left(B_d\left(\frac{1}{f_2^{liq}} - \frac{1}{f_2} \right) \right) = 1 - t_{tr} \tag{9}$$

The data presented in Fig. 2 inserted in Eq. (9) can be used to calculate t_{tr}. For linear polyethylene with $f_2 = 0.41–0.43$ and $f_2^{liq} \approx 0.80$ (Method I; ICC, IL and L are assumed to be penetrable phases), and with $f_2 = 0.44–0.46$ and $f_2^{liq} \approx 0.85$ (Method II; IL and L are assumed to be penetrable phases): $1 - t_{tr} \approx 0.7 - 3.4 \times 10^{-4}$. For branched polyethylene, depending on the degree of crystallinity, f_2 ranges from 0.045 to 0.081 (Method I) yielding $1 - t_{tr} \approx 2 \times 10^{-4} - 0.62$. For branched polyethylene with $v_{cc} = 0.20$, $1 - t_{tr} \approx 0.02$. It should be noted that one of the assumptions ($t_{int} \gg t_{liq}$; see Appendix B for definitions) is not valid for the branched polyethylene with low crystallinity, when $v_{cc} < 0.15$. The implication of the composite model is that in polyethylene with $v_{cc} > 0.15$, the penetrant molecules will spend almost all their time trapped at interfacial sites. Hence, the concentration of penetrant molecules will be higher in the interfacial component than in the liquid-like component. This paradox may be sorted out by considering that only a small part of a penetrant molecule is within the interfacial
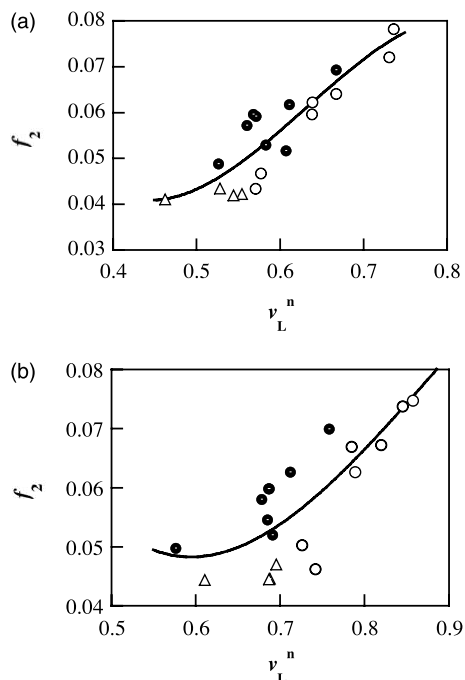
Fig. 7. Fractional free volume of the penetrable polymer fraction (f_2) as a function of volume fraction of the liquid-like component in the penetrable fraction of the polymer (v_L^n). Drawn after data from Neway et al. [9,15]. The continuous line is a third degree polynomial fit to the data. (a) Method 1: ICC, IL and L are penetrable phases; (b) Method II: IL and L are penetrable phases.

component and that the larger part is housed within the liquid-like component.

The difference in the free volume–crystallinity relationship between linear and branched polyethylene shown in Fig. 2 is given an explanation in Fig 7: f_2 shows a continuous change with the volume fraction of liquid-like component in the penetrable fraction (v_L^n) for both linear and branched polyethylene. The data obtained by method I (ICC, IL and L are penetrable phases) showed less scatter than those obtained by method II (IL and L are penetrable phases). The balance between liquid-like and interfacial components at a given crystallinity was thus different for linear and branched polyethylene; branched polyethylene had a higher proportion of liquid-like component. Method I provided a reasonably unified description of the data obtained for the different groups of materials (Fig. 7(a)). The significant scatter was not due to low accuracy in the determination of f_2. It was shown in a previous paper [9] that the uncertainty in the assessment of f_2 associated with the uncertainty in the determination of phase composition by Raman spectroscopy is negligible. The scatter in the data presented in Fig. 7(a) and (b) was due to the fairly large uncertainty in the assessment of v_L^n: the error in v_L^n has a maximum at low v_L^n: 10–15% (relative error) and 5–10% in the high v_L^n-range. The scatter in the data presented in Fig. 7(a) is well within these limits. The scatter in the data presented in Fig. 7(b) is, however, greater than predicted by the error analysis.

Method I, assuming ICC, IL and L to be penetrable phases, thus seems to give the most consistent data.

Although it is possible to find a unique relationship between f_2 and the composition of the penetrable phase according to Raman spectroscopy for a wide range of polyethylenes, including linear and branched polyethylene, the composite model is not yet proven to be correct.

4. Conclusions

Morphological data for a series of homogeneous poly(ethylene-*co*-octene)s obtained by differential scanning calorimetry and electron microscopy used as input data in the Fricke model to calculate the geometrical impedance factor showed the same trend with increasing crystallinity as the data obtained from *n*-hexane desorption. The high geometrical impedance factor shown by the low crystallinity samples was due to the presence of crystals with an unusually high crystal width-to-thickness ratio. The difference between linear and branched polyethylene with regard to fractional free volume–crystallinity data was due to a different balance between interfacial and liquid-like components in the two groups of material. A unified relationship, including data for both linear and branched polyethylene, was found between fractional free volume and phase composition of the penetrable phase including liquid-like, interfacial liquid and interfacial crystal core components.
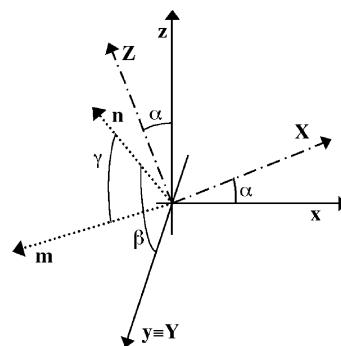
Fig. A1. Definition of Cartesian coordinate systems **xyz** and **XYZ**.

Appendix A. Conversion of average width of crystal lamellae in the image plane to the true average width of the crystal lamellae

Two Cartesian coordinate systems denoted **xyz** (unit vectors along the axes denoted **i**, **j** and **k**) and **XYZ** (unit vectors are **I**, **J** and **K**) are defined according to Fig. A1. The two coordinate systems have the same origin and $\mathbf{y} \equiv \mathbf{Y}$. The **x** and **z** axes can take different angles (denoted α) with respect to **X** and **Z** (Fig. A1). The **xy** plane is defined as the sectioning plane. The orientation of the crystal lamella is defined by the **XYZ** coordinate system: **X** is along the growth direction (crystallographic **b** axis). The lamella can 'rotate' about the **X**-axis; **n** represents the true width of the crystal lamella as a vector. Hence, the two orthogonal vectors **I** and **n** represent the fold surface. The angle between **n** and **J** is denoted β.

The vector **m** is defined as the projection of **n** on the plane **xy** along **X**. Hence, $|\mathbf{m}|$ represents the length of the edge-on view of a lamella with width $|\mathbf{n}|$. The angle between **n** and **m** is denoted γ. Hence:

$$|\mathbf{n}| = |\mathbf{m}| \cdot \cos \gamma \tag{A1}$$

The following expressions from standard mathematics relating the unit vectors of the two coordinate systems are useful in the derivation:

$$\mathbf{n} = \cos \beta \cdot \mathbf{j} + \sin \beta \cdot \mathbf{K} \tag{A2}$$

$$\mathbf{K} = -\sin \alpha \cdot \mathbf{i} + \cos \alpha \cdot \mathbf{k} \tag{A3}$$

Combination of Eqs. (A2) and (A3), yields the following expression:

$$\mathbf{n} = \cos \beta \cdot \mathbf{j} + \sin \beta \cdot (-\sin \alpha \cdot \mathbf{i} + \cos \alpha \cdot \mathbf{k}) \tag{A4}$$

Similarly, for vector **m**:

$$\mathbf{m} = \cos \gamma \cdot \mathbf{n} - \sin \gamma \cdot \mathbf{I} \tag{A5}$$

$$\mathbf{I} = \cos \alpha \cdot \mathbf{i} + \sin \alpha \cdot \mathbf{k} \tag{A6}$$

Combining Eqs. (A4–A6), yields:

$$\mathbf{m} = \cos \gamma \cdot (\cos \beta \cdot \mathbf{j} + \sin \beta \cdot (-\sin \alpha \cdot \mathbf{i} + \cos \alpha \cdot \mathbf{k}))$$
$$- \sin \gamma \cdot (\cos \alpha \cdot \mathbf{i} + \sin \alpha \cdot \mathbf{k}) \tag{A7}$$

The vector **m** is in the **xy** plane and its z component should, therefore, be zero. Hence:

$$\cos \alpha \cdot \sin \beta \cdot \cos \gamma - \sin \alpha \cdot \sin \gamma = 0 \tag{A8}$$

which can be rearranged to:

$$\tan \gamma = \frac{\cos \alpha \cdot \sin \beta}{\sin \alpha} \tag{A9}$$

Combining Eqs. (A1) and (A9) yields:

$$|\mathbf{n}| = |\mathbf{m}| \cdot \cos \left(\arctan \left(\frac{\cos \alpha \cdot \sin \beta}{\sin \alpha} \right) \right) \tag{A10}$$

Eq. (A10) relates $|\mathbf{n}|$ and $|\mathbf{m}|$ for a particular set of angles α and β. In order to obtain the relationship between the average projection (assuming all possible values of α and β), Eq. (A10) is integrated on $\alpha \in [t; \pi/2]$ with t approaching 0 (this is to avoid the singularity at $\alpha = 0$) and $\beta \in [0; \pi/2]$:

$$Q = \frac{4}{\pi^2}$$
$$\times \lim_{t \to 0} \int_{\alpha=t}^{\pi/2} \int_{\beta=0}^{\pi} \cos \left(\arctan \left(\frac{\cos \alpha \cdot \sin \beta}{\sin \alpha} \right) \right) d\alpha d\beta$$
$$= 0.74245 \tag{A11}$$

The integral was numerically solved using Mathematica®. The average lamellar width ($\langle W \rangle$) is obtained from:

$$\langle W \rangle = \langle L_{\mathrm{EO}} \rangle \cdot Q \tag{A12}$$

where L_{EO} is the average length of the edge on view of the lamella.

Appendix B. Deriving a relationship between fractional free volume and fractional time spent at interfacial sites (trapped state)

The diffusivity (D) is related to the square of the net average travelling distance $\langle \mathbf{r}^2 \rangle$ of a penetrant molecule in a material matrix according to Einstein [37]:

$$D = \frac{\langle \mathbf{r}^2 \rangle}{6t} \tag{B1}$$

where t is the time of the diffusive travel. Let us assume a system consisting of the following two components:

(i) a liquid-like phase in which the penetrant molecule moves relatively fast. The penetrant motion is characterized by the zero-concentration diffusivity $D_{\mathrm{c} \to 0}^{\mathrm{liq}}$;

(ii) a phase, here denoted the interfacial component, which allows very little penetrant motion. The penetrant diffusivity in the interfacial phase is set to zero.

The zero-concentration penetrant diffusivity of the liquid-like phase is according to Eq. (B1) given by:

$$D_{\mathrm{c} \to 0}^{\mathrm{liq}} = \frac{\langle \mathbf{r}^2 \rangle}{6t_{\mathrm{liq}}} \tag{B2}$$

where $\langle \mathbf{r}^2 \rangle_{\mathrm{liq}}$ is the travelling distance during time t_{liq}. The same travelling distance in the two-phase system requires a longer time: $t_{\mathrm{liq}} + t_{\mathrm{int}}$, where t_{int} is the time spent in the interfacial component. The effective zero-concentration penetrant diffusivity ($D_{\mathrm{c} \to 0}^{\mathrm{liq}}$) in this two-phase medium becomes:

$$D_{c\to0}^{\text{liq}} = \frac{\langle \mathbf{r}^2 \rangle_{\text{liq}}}{6(t_{\text{liq}} + t_{\text{int}})} \tag{B3}$$

The following expression is obtained by combining Eqs. (B2) and (B3):

$$\frac{D_{c\to0}^{\text{eff}}}{D_{c\to0}^{\text{liq}}} = \frac{t_{\text{liq}}}{t_{\text{liq}} + t_{\text{int}}} \tag{B4}$$

It is assumed that the penetrant molecule spends the great majority of its time in the interfacial component (trapped state), i.e. $t_{\text{int}} \gg t_{\text{liq}}$. Eq. (B4) can then be simplified to:

$$\frac{D_{c\to0}^{\text{eff}}}{D_{c\to0}^{\text{liq}}} = \frac{t_{\text{liq}}}{t_{\text{int}}} = \frac{t - t_{\text{int}}}{t_{\text{int}}} \tag{B5}$$

where $t = t_{\text{liq}} + t_{\text{int}}$ is the total time for diffusion. The fractional time (t_{tr}) that the penetrant molecule spends in the interfacial component, i.e. in the trapped state, is defined:

$$t_{\text{tr}} = \frac{t_{\text{int}}}{t} \tag{B6}$$

The following expression is obtained by inserting Eq. (B6) in Eq. (B5) and by considering that $t_{\text{int}} \gg t_{\text{liq}}$:

$$\frac{D_{c\to0}^{\text{eff}}}{D_{c\to0}^{\text{liq}}} = 1 - t_{\text{tr}} \tag{B7}$$

The zero-concentration diffusivity ($D_{c\to0}$) is according to the Cohen–Turnbull–Fujita model [4–6] given by:

$$D_{c\to0} = \frac{K}{\tau} \times \exp(-B_{\text{d}}/f_2) \tag{B8}$$

where K is a constant independent of the degree of crystallinity, τ is the geometrical impedance factor, B_{d} is a constant that depends only on the size and shape of the penetrant molecule and f_2 is the fractional free volume of the polymer. Note that $A = K/\tau$, cf. Eqs. (B8) and (2). The zero-concentration diffusivity of the liquid-like phase ($D_{c\to0}^{\text{liq}}$) is, since $\tau = 1$ according to the definition (Eq. (1), given by:

$$D_{c\to0}^{\text{liq}} = K \times \exp(-B_{\text{d}}/f_2^{\text{liq}}) \tag{B9}$$

where f_2^{liq} is the fractional free volume of the liquid-like polymer. The effective diffusivity disregarding the geometrical impedance factor is then given by:

$$D_{c\to0}^{\text{eff}} = D_{c\to0} \times \tau = K \times \exp(-B_{\text{d}}/f_2) \tag{B10}$$

Combining Eqs. (B9) and (B10) yields:

$$\frac{D_{c\to0}^{\text{eff}}}{D_{c\to0}^{\text{liq}}} = \frac{\exp(-B_{\text{d}}/f_2)}{\exp(-B_{\text{d}}/f_2^{\text{liq}})} = \exp\left(B_{\text{d}}\left(\frac{1}{f_2^{\text{liq}}} - \frac{1}{f_2}\right)\right) \tag{B11}$$

By combining Eqs. (B7) and (B11), the following expression is obtained:

$$\exp\left(B_{\text{d}}\left(\frac{1}{f_2^{\text{liq}}} - \frac{1}{f_2}\right)\right) = 1 - t_{\text{tr}} \tag{B12}$$

References

[1] Simha R, Carri G. J Polym Sci, Polym Phys 1994;32:2645.
[2] Kitamaru R, Horii F, Hyon S-H. J Polym Sci, Polym Phys 1977;15: 821.
[3] Mutter R, Stille W, Strobl G. J Polym Sci, Polym Phys 1993;31:99.
[4] Cohen MH, Turnbull D. J Chem Phys 1959;31:1164.
[5] Turnbull D, Cohen MH. J Chem Phys 1970;52:3038.
[6] Fujita H. Fortschr Hochpolym Forsch 1961;3:1.
[7] Kulkarni SS, Stern SA. J Polym Sci, Polym Phys 1983;21:441.
[8] Hedenqvist M, Angelstok AA, Edsberg L, Larsson PT, Gedde UW. Polymer 1996;37:2887.
[9] Neway B, Hedenqvist MS, Gedde UW. Polymer 2003;44:4003.
[10] Neway B, Hedenqvist MS, Mathot VBF, Gedde UW. Polymer 2001; 42:5307.
[11] Fels M, Huang RYM. J Appl Polym Sci 1970;14:523.
[12] Fleischer G. Coll Polym Sci 1984;262:919.
[13] Doolittle AK. J Appl Phys 1951;22:1471.
[14] Williams ML, Landel RF, Ferry JD. J Am Chem Soc 1955;77:3701.
[15] Neway B, Westberg Å, Mattozzi A, Hedenqvist MS, Giacinti Baschetti M, Mathot VBF, Gedde UW. Polymer 2004;45:3913.
[16] Gray AP. Thermochim Acta 1970;1:563.
[17] Flory PJ, Vrij A. J Am Chem Soc 1963;85:3548.
[18] Wunderlich B, Baur H. Adv Polym Sci 1970;7:151.
[19] Gedde UW. Polymer physics. London: Chapman & Hall; 1995.
[20] Pakula T, Kryszewski M, Soukup Z. Eur Polym J 1976;12:41.
[21] Shahin MM, Olley RH, Blissett MJ. J Polym Sci, Polym Phys 1999; 37:2279.
[22] Hoffman JD, Frolen LJ, Ross GS, Lauritzen JI. J Res Natl Bur Std—A Phys Chem 1975;(79A):671.
[23] Busing WR. Macromolecules 1990;23:4608.
[24] Defoor F, Groeninckx G, Reynaers H, Schouterden P, Van der Heijden B. Macromolecules 1993;26:2575.
[25] Flory PJ. Trans Faraday Soc 1955;51:848.
[26] Hay JN, Zhou X-Q. Polymer 1993;34:1002.
[27] Hosoda S, Nomura H, Gotoh Y, Kihara H. Polymer 1990;31:1999.
[28] Mathur SC, Mattice WC. Macromolecules 1987;20:2165.
[29] Li Y, Akpulo YA. Macromolecules 2004;37:7265.
[30] Darras O, Séguéla R. Polymer 1993;34:2946.
[31] Michaels AS, Bixler HJ. J Polym Sci 1961;5:413.
[32] Fricke H. Phys Rev 1924;24:575.
[33] Hadgett PM, Goldbeck-Wood G, Windle AH. Polymer 2000;(41): 6151.
[34] Mattozzi A, Serralunga P, Hedenqvist MS, Gedde UW. Polymer, submitted.
[35] Boyd RH. Polym Eng Sci 1979;19:1010.
[36] Vonk CG, Pijpers AP. J Polym Sci, Polym Phys 1985;23:2517.
[37] Einstein A. Ann Phys 1905;17:549.